Monthly Notices
of the
ROYAL ASTRONOMICAL SOCIETY

MNRAS **494,** 1936–1945 (2020) doi:10.1093/mnras/staa762

All-sky angular power spectrum – I. Estimating brightness temperature fluctuations using the 150-MHz TGSS survey

Samir Choudhuri,[1,2]★ Abhik Ghosh,[3,4,5] Nirupam Roy,[6] Somnath Bharadwaj,[7] Huib. T. Intema[8] and Sk. Saiyad Ali[9]

[1]*Astronomy Unit, Queen Mary University of London, Mile End Road, London E1 4NS, UK*
[2]*National Centre For Radio Astrophysics, Post Bag 3, Ganeshkhind, Pune 411 007, India*
[3]*Department of Physics, Banwarilal Bhalotia College, GT Rd, Ushagram, Asansol, West Bengal, India*
[4]*Department of Physics and Astronomy, University of the Western Cape, Robert Sobukwe Road, Bellville 7535, South Africa*
[5]*The South African Radio Astronomy Observatory (SARAO), 2 Fir Street, Black River Park, Observatory, Cape Town 7925, South Africa*
[6]*Department of Physics, Indian Institute of Science, Bangalore 560012, India*
[7]*Department of Physics and Centre for Theoretical Studies, IIT Kharagpur, Kharagpur 721 302, India*
[8]*Leiden Observatory, Leiden University, Niels Bohrweg 2, NL-2333CA, Leiden, The Netherlands*
[9]*Department of Physics, Jadavpur University, Kolkata 700032, India*

Accepted 2020 March 16. Received 2020 February 28; in original form 2019 October 4

ABSTRACT

Measurements of the Galactic synchrotron emission are important for the 21-cm studies of the epoch of reionization. The study of synchrotron emission is also useful for quantifying the fluctuations in the magnetic field and the cosmic-ray electron density of the turbulent interstellar medium (ISM) of our Galaxy. Here, we present the all-sky angular power spectrum (C_ℓ) measurements of the diffuse synchrotron emission obtained using the TIFR GMRT Sky Survey (TGSS) at 150 MHz. We estimate C_ℓ using visibility data both before and after subtracting the modelled point sources. The amplitude of the measured C_ℓ decreases significantly after subtracting the point sources, and it is slightly higher in the Galactic plane for the residual data. The residual C_ℓ is most likely to be dominated by the Galactic synchrotron emission. The amplitude of the residual C_ℓ decreases significantly away from the Galactic plane. We find that the measurements are quite symmetric in the Northern and Southern hemispheres except in the latitude range $15^\circ - 30^\circ$, which is the transition region from the disc-dominated to the diffuse halo-dominated region. A comparison between this interferometric measurement and the scaled version of the Haslam rms map at 150 MHz shows that the correlation coefficient (r) is greater than 0.5 for most of the latitude ranges considered here. This indicates that the TGSS is quite sensitive to the diffuse Galactic synchrotron radiation.

Key words: methods: data analysis – methods: statistical – techniques: interferometric – dark ages, reionization, first stars – radio continuum: galaxies – radio continuum: general.

1 INTRODUCTION

The redshifted 21-cm signal from neutral hydrogen (H I) is perceived to be one of the most promising probes of the epoch of reionization (EoR) (see Furlanetto, Oh & Briggs 2006; Morales & Wyithe 2010; Pritchard & Loeb 2012; Mellema et al. 2013 for reviews). The hydrogen in the Universe changes its phase from the neutral to the ionized state in this epoch, and many issues such as the exact time and duration of reionization, and the sources responsible for this process are still unresolved. Several ongoing and future radio telescopes such as the Low Frequency Array (LOFAR[1], var Haarlem et al. 2013), the Murchison Wide-field Array (MWA[2], Bowman et al. 2013), the Square Kilometer Array (SKA1 LOW[3], Koopmans et al. 2015) and the Hydrogen Epoch of Reionization Array (HERA[4], DeBoer et al. 2017), as well the Giant Metrewave Radio Telescope (GMRT [5]; Swarup et al. 1991; Paciga et al. 2013) are seeking to measure the 21-cm signal from the EoR.

★ E-mail: s.choudhuri@qmul.ac.uk

[1]http://www.lofar.org/
[2]http://www.mwatelescope.org
[3]http://www.skatelescope.org/
[4]http://reionization.org/
[5]http://www.gmrt.ncra.tifr.res.in

The presence of strong astrophysical foregrounds that are 4–5 orders of magnitude brighter than the expected 21-cm signal (Shaver et al. 1999; Di Matteo et al. 2002; Santos et al. 2005; Ali, Bharadwaj & Chengalur 2008; Paciga et al. 2011; Ghosh et al. 2011) poses a significant challenge for the detection of the EoR 21-cm signal. The major foreground components include extragalactic radio point sources, the diffuse Galactic synchrotron emission (DGSE), and Galactic and extragalactic free–free emission. The extragalactic point sources are the most dominant foreground components at the angular scales that are relevant for telescopes such as LOFAR and SKA (Ali, Bharadwaj & Chengalur 2008; Ghosh et al. 2012). The DGSE dominates at large angular scales, >10 arcmin, after point sources are subtracted at the level of ∼10–20 mJy (Bernardi et al. 2009; Ghosh et al. 2012; Iacobelli et al. 2013; Choudhuri et al. 2017a).

The DGSE is produced by cosmic-ray electrons spiralling in the Galactic magnetic field lines (Ginzburg & Syrovatskii 1969; Rybicki & Lightman 1979). A precise characterization and a detailed understanding of the DGSE are needed to remove foregrounds in 21-cm experiments reliably. Furthermore, the angular fluctuations of the DGSE are directly related to the fluctuations in the magnetic field and to the fluctuations in the cosmic-ray electron density of the turbulent interstellar medium (ISM) of our Galaxy (Cho & Lazarian 2008; Waelkens et al. 2009; Regis 2011; Lazarian & Pogosyan 2012; Iacobelli et al. 2013), and these relationships are not very well understood at present. Lazarian & Pogosyan (2012) have suggested avenues for quantitative studies of magnetic turbulence in our Galaxy and beyond using observations of the synchrotron emission, and they have also outlined how synchrotron foreground emission could be separated from the cosmological signal, namely from the cosmic microwave background (CMB) or from highly redshifted H I 21-cm emission.

Several observations spanning a wide range of frequencies have characterized various aspects of the DGSE (Haslam et al. 1981, 1982; Reich 1982; Reich & Reich 1988; Jonas, Baart & Nicolson 1998; Ellingson et al. 2013). Guzmán et al. (2011) produced an all-sky spectral index map of the DGSE between 45 and 408 MHz using their own all-sky map at 45 MHz, the 45-MHz southern and northern sky maps (Alvarez et al. 1997; Maeda et al. 1999) and the 408-MHz all-sky map (Haslam et al. 1981, 1982). The Global Sky Model (hereafter, GSM) for the diffuse Galactic emission temperature map has been developed in the frequency range 10 MHz to 94 GHz based on the 11 most accurate data sets using principal component analysis (de Oliveira-Costa et al. 2008). Zheng et al. (2017) produced an improved GSM of the diffuse Galactic radio emission from 10 MHz to 5 THz, which includes 29 sky maps. These types of model are very useful for understanding the Galactic foreground contributions in the wide-band CMB and cosmological 21-cm H I observations.

The statistical properties of the DGSE can be quantified in terms of the angular power spectrum C_ℓ. Various authors have used the above-mentioned all-sky observations to estimate the statistical properties of the DGSE for a wide range of frequencies (Tegmark & Efstathiou 1996; Bouchet & Gispert 1999; Giardino et al. 2001, 2002; Bennett et al. 2003). The C_ℓ of the DGSE intensity fluctuations over large portions of the sky can be modelled by a power law, namely $C_\ell \propto \ell^{-\beta}$ (Tegmark et al. 2000; Baccigalupi et al. 2001). La Porta et al. (2008) analysed the 408-MHz Haslam map (Haslam et al. 1981, 1982) and the 1420-MHz survey data (Reich 1982; Reich & Reich 1986; Reich, Testori & Reich 2001) separately to measure the C_ℓ of the DGSE and found β values in the range 2.6–3.0 down to the angular multipoles of $\ell = 200$ and 300 at 408 and 1420 MHz, respectively. These studies show that β steepen (or increases) towards higher Galactic latitudes.

The properties of the angular power spectrum of the DGSE are not well quantified at the frequencies and angular scales relevant for detecting the cosmological 21-cm signal from the EoR. Parsons et al. (2010) presented an all-sky synthesized map and estimated the C_ℓ between 139 and 174 MHz. It has also been measured in a few small fields at low Galactic latitude $|b| < 14^\circ$ in the frequency range 150–160 MHz (Bernardi et al. 2009, 2010; Ghosh et al. 2012; Iacobelli et al. 2013; Choudhuri et al. 2017a). Bernardi et al. (2009) and Ghosh et al. (2012) analysed, respectively, 150-MHz WSRT and GMRT observations, where they respectively found $\beta = 2.2 \pm 0.3$ and $\beta = 2.34 \pm 0.28$ up to $\ell = 900$. Iacobelli et al. (2013) measured the C_ℓ of the DGSE at 160 MHz using LOFAR data and reported that the angular power spectrum has a slope $\beta \approx 1.8$ down to the angular multipoles ℓ of 1300. In an earlier paper (Choudhuri et al. 2017a), we analysed two fields from the TIFR GMRT Sky Survey (TGSS)-ADR1 survey at 150 MHz (Intema et al. 2017) and measured the C_ℓ of the DGSE across the ℓ range $240 \leq \ell \leq 500$, finding that the values of β are 2.8 ± 0.3 and 2.2 ± 0.4, respectively, in the two fields. Recently, Chakraborty et al. (2019) measured the C_ℓ in the ELAIS-N1 field and found β values consistent with earlier measurements. All of these results are restricted to a small portion of the sky $\leq 6^\circ \times 6^\circ$.

The GMRT field of view has a full width at half-maximum (FWHM) of $3^\circ.1$[6] at 150 MHz. The TGSS (Sirothia et al. 2014) contains observations from 5336 pointings covering a large fraction (90 per cent) of the total sky in the declination range $\delta > -55^\circ$. Here we have used the first alternative data release (ADR1) of the TGSS, which was calibrated and processed by Intema et al. (2017). We applied the visibility-based tapered gridded estimator (TGE) (Choudhuri et al. 2016b) to estimate C_ℓ individually for all the TGSS pointings. This results in estimates of C_ℓ spanning the ℓ range of approximately $100 \leq \ell \leq 4000$ in 3893 pointing directions. We removed some pointings owing to large system noise or the presence of strong radio frequency interference (RFI). The analysis was carried out both before and after source subtraction, with three main aims. The first aim is to characterize the fluctuations in the sky brightness directly for different pointing directions on the sky. This provides a direct estimate of the foregrounds for EoR 21-cm observations centred at different directions of the sky.

Source subtraction (Ali et al. 2008; Ghosh et al. 2012; Beardsley et al. 2016; Gehlot et al. 2019; Kerrigan et al. 2018) offers a technique for foreground mitigation; it is, however, limited by our ability to accurately calibrate the visibility data and model the sources. The TGSS ADR1 uses a novel method to incorporate direction-dependent (DD) calibration in all the data sets. It generates a model of the ionosphere using a few strong sources present in that field and corrects the phase due to this ionospheric distortion. It helps to model the extragalactic point sources with more accuracy. We removed the discrete point sources above 5σ (σ is below 5mJy for the majority of the pointings). The second aim here is thus to investigate the foreground reduction that is actually achieved through source subtraction in different observing directions of the sky.

Finally, we attempt to use the residual data after source subtraction to quantify the statistical properties of the DGSE, which is expected to be the dominant foreground contribution after source subtraction.

[6] http://gmrt.ncra.tifr.res.in/

A brief outline of the paper is as follows. In Section 2, we briefly describe the GMRT data and the method of analysis. In Section 3, we present our measurement of the angular power spectrum before and after point-source subtraction and discuss the quantum of drop that occurs in different directions owing to the efficacy of point-source removal. A comparison with single-dish observations is presented in Section 4. Finally, we summarize and conclude in Section 5. In a companion paper, we plan to provide details of the power-law fitting, the variation of the power-law index, and the interpretation of the C_ℓ of the DGSE from residual data.

2 METHODOLOGY

The TGSS (Sirothia et al. 2014) is the first all-sky continuum survey at a low frequency that is directly relevant for EoR studies. The observing frequency for this survey is 150 MHz with a bandwidth of 16.7 MHz. Although the data were recorded with full polarization, we used only Stokes I for this work. The total survey area was divided into 5336 individual pointings on an approximately hexagonal grid, and the integration time for each pointing was about 15 min. Here we summarize the methodology from data reduction to power spectrum estimation. We divide the total process into two parts: the data analysis and the power spectrum estimation.

The TGSS data were analysed using a fully automated pipeline, the Source Peeling and Atmospheric Modeling (SPAM) package (Intema et al. 2009; Intema 2014). This pipeline consists of a pre-processing and a main-pipeline component. The pre-processing part converts the raw data into pre-calibrated visibilities for each pointing. Flagging, gain calibration, bandpass calibrations and also the correction for the system temperature variation are incorporated in this part in order to improve the quality of the data. Finally, the main-pipeline section converts the pre-calibrated visibility into the final calibrated data set and the final Stokes-I image for each pointing. Here, both the direction-independent calibration and the DD calibration are applied to the data. Details of the analysis can be found in Intema et al. (2017). The background rms noise is below 5mJy for the majority of the pointings, with an angular resolution of 25 arcsec $\times$ 25 arcsec (or 25 arcsec $\times$ 25 arcsec/cos(Dec. $-$ 19°) for pointings south of 19° Dec. The discrete point sources above a 5σ threshold value have been removed in the final residual data sets. In this paper, we used the data both before and after point-source subtraction to estimate the angular power spectrum. In our earlier paper (Choudhuri et al. 2017a), we presented results for two fields located at galactic coordinates of (9°, +10°) and (15°, −11°). The present work is an extension of our earlier work, in that we now analyse the entire sky region covered by the TGSS.

In this paper, we use the TGE (Choudhuri et al. 2016b) to estimate the angular power spectrum C_ℓ. A brief summary of the salient features of the TGE is as follows. The TGE has three main characteristics: (i) it uses the gridded visibility data to reduce the computation; (ii) it tapers the sky response from the outer region of the primary beam, where it is highly frequency-dependent; and (iii) it subtracts the noise bias to give an unbiased estimate of the true sky signal. We divided the whole 'uv' plane in a rectangular grid. We convolved the measured visibilities around each grid point with the Fourier transform of a window function, which will effectively taper the sky response. The convolved visibility $\mathcal{V}_{cg}$ at every grid point g can be written as

$$\mathcal{V}_{cg} = \sum_i \tilde{w}(\mathbf{U}_g - \mathbf{U}_i)\,\mathcal{V}_i, \tag{1}$$

where $\tilde{w}(\mathbf{U})$ is the Fourier transform of the tapering window function $\mathcal{W}(\theta)$, $\mathbf{U}_g$ refers to the baseline of different grid points, and $\mathcal{V}_i$ is the visibility measured at baseline $\mathbf{U}_i$. We collapsed the visibility measurements in different frequency channels after scaling each baseline to the appropriate frequency. The TGE correlates the convolved visibilities at each grid point to estimate the C_ℓ. As noted, it subtracts the self-correlation of the measured visibilities around each grid point, which is responsible for the noise bias. The mathematical expression for the TGE is given by (Choudhuri et al. 2016b, equation 17)

$$\hat{E}_g = M_g^{-1}\left(\mid \mathcal{V}_{cg} \mid^2 - \sum_i \mid \tilde{w}(\mathbf{U}_g - \mathbf{U}_i) \mid^2 \mid \mathcal{V}_i \mid^2\right), \tag{2}$$

where M_g is the normalizing factor, which we calculated using simulated visibilities corresponding to a unit angular power spectrum (details in Choudhuri et al. 2016b). We assumed that the signal is isotropic, enabling us to average the C_ℓ measurements over an annular region to increase the signal-to-noise ratio. We used equations (19) and (25) of Choudhuri et al. (2016b) to estimate the C_ℓ and its variance in bins of equal logarithmic interval in ℓ, and we divided the whole ℓ range into 25 equally spaced logarithmic bins. The estimator has been already validated using realistic simulations of GMRT 150-MHz observations (Choudhuri et al. 2016b). In Choudhuri et al. (2016a), we included point sources in a large region of the sky and showed that the TGE effectively suppresses the point-source contribution from the outer regions of the primary beam.

3 RESULTS

In this section, we present the results for the angular power spectrum measurements before and after subtracting the point sources from the calibrated visibility data. We removed all fields that are dominated by the system noise or that have strong RFI. Finally, out of the 5336 TGSS fields, we present the results for 3893 fields that we expect to be dominated by the sky signal.

Fig. 1 shows the measured C_ℓ before and after point-source subtraction for four representative fields, with galactic coordinates (l, b) = (127.24, −9.25), (209.47, −9.88), (200.10, 14.09) and (287.47, 23.56). The results for all of the 3893 TGSS pointings that have been analysed here are available online.[7] The upper curves in these figures show C_ℓ with 1σ error bars before point-source subtraction. Here the values of C_ℓ are in the range 10^4-10^5 mK^2, and the curves are more or less flat. The sky signal here is predicted (Ali et al. 2008) to be dominated by the Poisson fluctuations of the point-source distribution, and the nearly flat C_ℓ is roughly consistent with this prediction. At low ℓ, the measured C_ℓ is affected by the convolution with the tapering window function and the antenna's primary beam pattern. As shown in fig. 2 of Choudhuri et al. (2017a), this convolution becomes important at $\ell < 240$. Furthermore, the clustering of the point sources starts to become important at the lower ℓ values.

Point sources with flux above a threshold flux $S_{\rm cut}$ were subtracted from the data. Here $S_{\rm cut} = 5\,\sigma$, where σ is the rms noise, which varies from pointing to pointing and is below 5 mJy for the majority of the pointings (Intema et al. 2017). The lower curves in Fig. 1 show the measured C_ℓ with 1σ error bars after subtracting the point sources from the data. It can be seen that the values of C_ℓ at

[7] http://www.physics.iisc.ernet.in/~nroy/plot_html

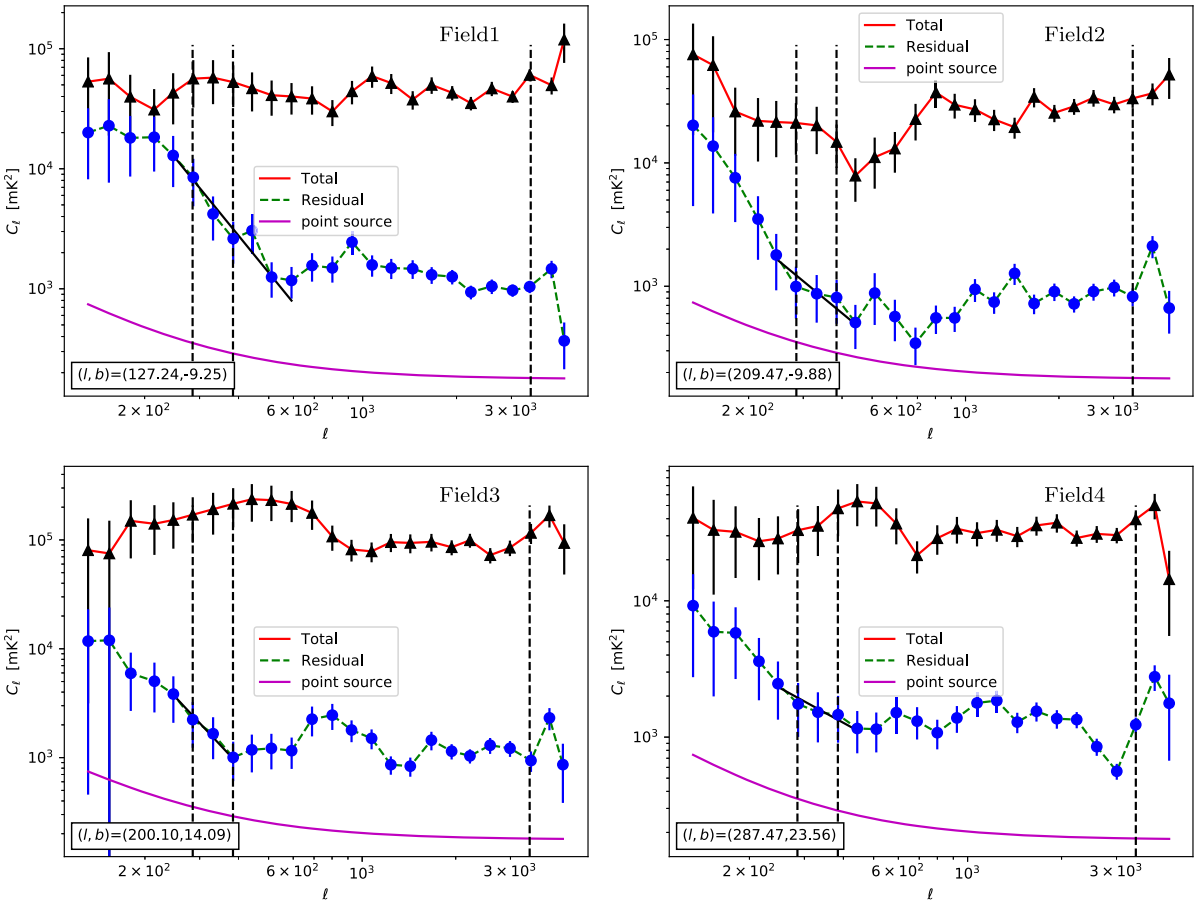

Figure 1. The estimated angular power spectra C_ℓ with 1σ error bars for four representative fields with different galactic coordinates. The upper (red solid line and 1 sigma error bar with black upper triangles) and lower curves (green dashed and 1 sigma error bar with blue circles) are for before and after point-source subtraction, respectively. The three dashed vertical lines show the values of ℓ that we use in Figs 2 and 3. The black solid line in each panel shows the best-fit power law for the measured C_ℓ (details in the text). The magenta line shows the C_ℓ model prediction due to unsubtracted point sources below 50 mJy.

large ℓ decrease substantially after the point sources are removed. The C_ℓ of the residual data shows a nearly flat nature, with values of $\sim 10^3$ mK^2 at $\ell > 700$. We believe that this is predominantly the contribution from the Poisson fluctuations of the residual point sources that have fluxes $S < S_{\rm cut}$. The fact that C_ℓ at large ℓ decreases by a factor of nearly 100 after the point sources have been subtracted is a clear indication that the original data are dominated by point sources. In Fig. 1, the magenta line shows the total C_ℓ prediction resulting from the clustering and the Poisson part of the residual point sources below a threshold flux density of 50 mJy. For this model prediction, we used a source count estimated from Intema et al. (2017) and the angular correlation function (in the range of $0.^\circ1$ to 1°) derived from Dolfi et al. (2019). It can be seen that at higher ℓ, the model C_ℓ is also dominated by the Poisson fluctuations of residual point sources and the value is an order of magnitude lower than the measured one. We saw a similar behaviour in our earlier TGSS angular power spectrum analysis (Choudhuri et al. 2017a). It may be because (i) there are significant residual imaging artefacts around the bright source ($S > S_{\rm cut}$) that were subtracted, and/or (ii) the actual source distribution is in excess of the predictions by the TGSS survey at lower flux ranges. Similar findings have recently been reported at the higher frequency of the 1.28-GHz MeerKAT DEEP2 Image, with Mauch et al. (2020) finding that the model prediction lies significantly below the observed source counts in the low flux range. In the lower ℓ range, we find that the values of the measured C_ℓ after point-source subtraction decrease with increasing ℓ and show a power-law-like behaviour (at $\ell < 700$). The predicted C_ℓ due to the clustering point sources at lower ℓ values also follows a power law in this range, but the amplitude is, in general, much lower than the residual C_ℓ (Fig. 1). We expect the C_ℓ measured here to be dominated by the diffuse Galactic synchrotron emission. The TGSS observations can probe angular scales in the range $0.^\circ045$ to $1.^\circ2$; however, because of the convolution of the primary beam and the residual point sources, we are limited to the range $0.^\circ3$ to $0.^\circ8$ for the DGSE measurements. As discussed in several previous studies (Bernardi et al. 2009; Ghosh et al. 2012; Iacobelli et al. 2013; Choudhuri et al. 2017a), it is possible to fit C_ℓ with a power law $A(1000/\ell)^\beta$ in this ℓ range.

We present the results for the power-law fitting in Fig. 1 for the four representative fields. The black solid line in each panel shows the best-fit power law in the ℓ range ($\ell_{\rm min}$, $\ell_{\rm max}$). Here we use $\ell_{\rm min} = 240$, because convolution becomes important at lower ℓ ranges, and $\ell_{\rm max} = 600$, 500, 400 and 450 for Field 1 to Field 4, respectively. For $\ell > \ell_{\rm max}$, the residual point sources and other systematic errors dominate, and hence we exclude this ℓ range in our fitting. The best-fitted values of the parameters are $(A, \beta) = (150 \pm 56, 3.2 \pm 0.3)$, $(90 \pm 50, 2.1 \pm 0.4)$, $(53 \pm 20, 3 \pm 0.3)$ and $(403 \pm 106, 1.3 \pm 0.2)$ for Field 1 to Field 4, respectively. The power-law fitting is done

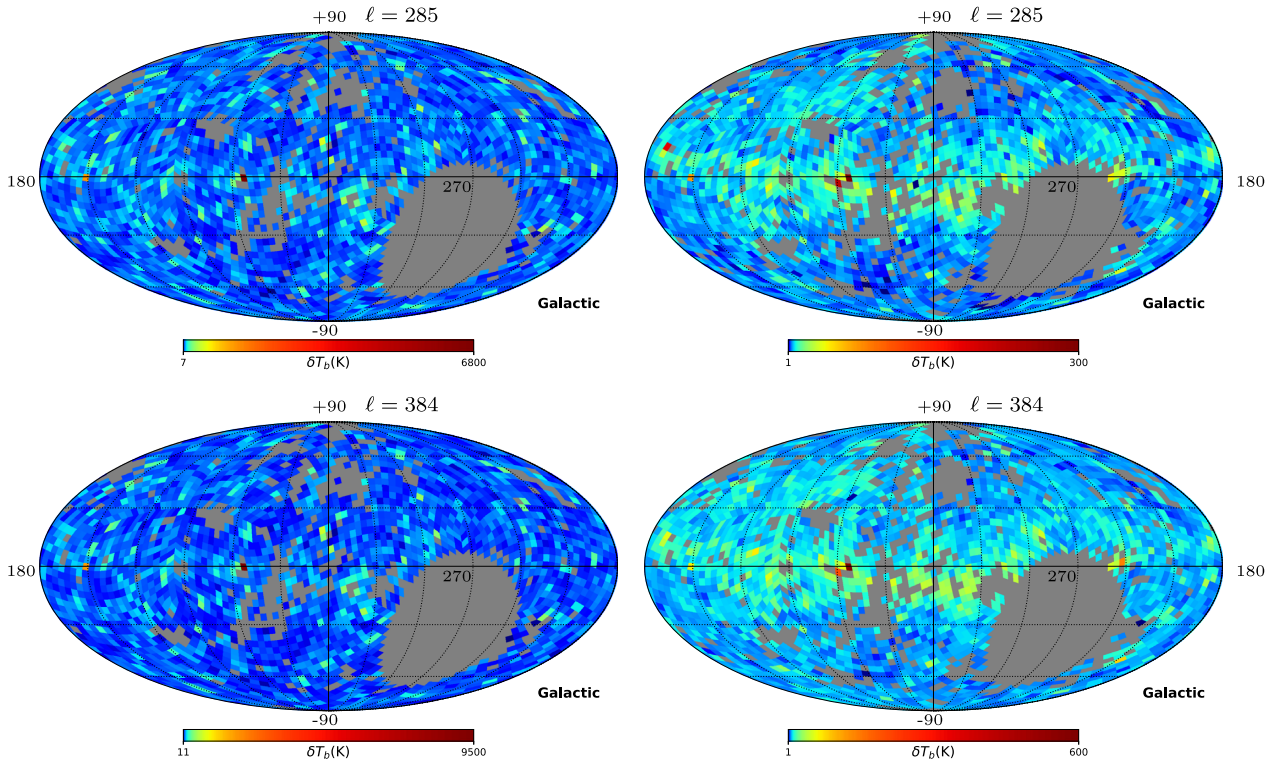

Figure 2. The rms fluctuations of the brightness temperature ($\delta T_{\rm b}$) all over the sky at various angular scales. The upper and lower panels are for $\ell = 285$ ($\sim 0\overset{\circ}{.}63$) and 384 ($\sim 0\overset{\circ}{.}47$), respectively. The left and right panels show the values of $\delta T_{\rm b}$ before and after subtracting the point sources from the data, respectively.

over a narrow range; however, that is what we can realistically do with the current data. So, the power-law power spectrum for the DGSE is an ansatz here, and the power-law index (β) under that assumption is consistent with earlier reported results (Choudhuri et al. 2017a) except for Field 4. The modelling of these four fields is in addition to that of the two other TGSS fields reported in our earlier paper (Choudhuri et al. 2017a). The details of the power-law fitting, the variation of the power-law index across different directions in the sky and the interpretation of the residual C_ℓs will be presented in a companion paper. For the present purpose, it suffices to note that for the residual data the DGSE dominates the measured C_ℓ at low ℓ (<700), whereas the residual point sources dominate at large ℓ.

We next consider the rms fluctuations of the brightness temperature $\delta T_{\rm b} = \sqrt{\ell(\ell+1)C_\ell/2\pi}$ at various ℓ values, each of which corresponds to a different angular scale. Fig. 2 shows how $\delta T_{\rm b}$ varies across different pointing directions in the sky. Here, we take the mean $\delta T_{\rm b}$ for all the TGSS pointings that fall into a particular HEALPix[8] (Górski et al. 2005) pixel. The upper and lower panels correspond to $\ell = 285$ ($\sim 0\overset{\circ}{.}63$) and 384 ($\sim 0\overset{\circ}{.}47$), respectively, whereas the left and right panels respectively correspond to before and after point-source subtraction. For both the multipoles shown here, we expect the signal to be dominated by the DGSE after point-source subtraction. The grey circular regions in the lower right part of these images have no data points as they correspond to the declination range (Dec. $< -53^\circ$) that is not covered by the TGSS. We also note that a few grey pixels distributed throughout the images were discarded as these correspond to pointings that were not included in our analysis because of either large system noise or RFI. In the left panels of Fig. 2, it can be seen that the distribution of $\delta T_{\rm b}$ is almost isotropic, with values in the range of a few hundred kelvin. The $\delta T_{\rm b}$ here is mainly due to the Poisson fluctuations of the extragalactic point sources. The sources, being cosmological in origin, are expected to have an isotropic distribution on the sky. In contrast, considering the right panels, which show the values of $\delta T_{\rm b}$ for the residual data for which all the discrete point sources have been removed, we see that the $\delta T_{\rm b}$ values are somewhat larger near the Galactic plane and decrease away from the Galactic plane. The values of $\delta T_{\rm b}$ vary in the range of a few tens of kelvin. We believe that the residual C_ℓ is most likely to be dominated by the Galactic synchrotron emission. In the Galactic plane, however, there will be an additional contribution from the residual thermal emission from H II regions, and also from the residual non-thermal emission from supernova remnants.

The measured C_ℓ for the DGSE decreases as a power law ($C_\ell \propto \ell^{-\beta}$) (Bernardi et al. 2009; Ghosh et al. 2012). In our earlier study with TGSS, we observed the same power-law nature of the C_ℓ as a function of ℓ (Choudhuri et al. 2017a). In Choudhuri et al. (2017a), we also found that the amplitude of the residual C_ℓ becomes almost constant at $\ell > \ell_{\rm max}$ (~ 550). We believe that this angular multipole range ($\ell > \ell_{\rm max}$) is dominated mainly by the the Poisson fluctuations of the residual point sources with flux values below $S_{\rm cut}$. In the four panels of Fig. 1, the characteristics of all the residual C_ℓ (green dotted curves) are similar to those in Choudhuri et al. (2017a). We can use the residual C_ℓ at large ℓ to set an upper limit on the DGSE at smaller angular scales. In Fig. 3, we show the variation of $\delta T_{\rm b}$ at $\ell = 3459$ ($\sim 3'$) after subtracting the point sources. We find that the residual map is almost isotropic at $\ell = 3459$, and the derived brightness temperature varies in the range

[8] http://healpix.sourceforge.net

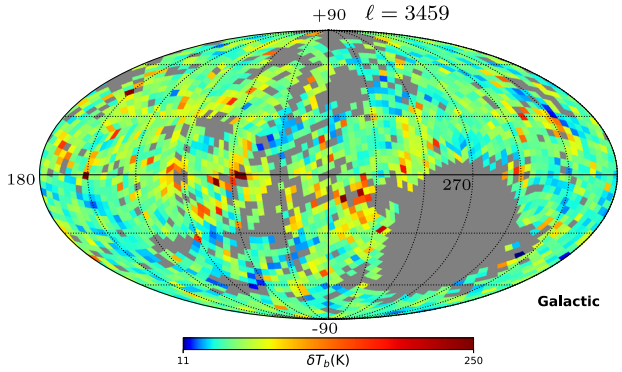

Figure 3. The distribution of δT_b at a small angular scale $\ell = 3459$ ($\sim 0.^{\circ}052$). The values of δT_b are almost isotropic, varying mostly within a range of 50−100 K. The small number of bright pixels in the map are might be caused by the presence of strong bright A-team sources that were not properly modelled and removed.

10−100 K. In comparison, the right panels of Fig. 2 show the values δT_b, which are larger in the Galactic plane. This is due to the DGSE, which dominates at those ℓ values ($\ell = 285$ and 383) shown in that figure. In addition, there are a few bright pixels in Fig. 3 that might be caused by the deconvolution error associated with bright A-team sources in the sky (> 300 Jy) (such as Cas A ($l = 111.734$, $b = -02.129$), Cygnus A ($l = 76.1898$, $b = +05.755$), Hydra A ($l = 242.925$, $b = +25.092$) etc. (Intema et al. 2017)). As mentioned earlier, the residual contribution from the H II regions and supernova remnants may also contribute in the Galactic plane.

We assume that the measured C_ℓs in a particular galactic latitude range are an independent realization of an underlying statistical distribution. Here, we quantify the statistical distribution of C_ℓ through the histogram of the C_ℓ values. In Fig. 4, we plot the histogram of the measured C_ℓ in various ranges of galactic latitude. We considered only $\ell = 384$, which is dominated mostly by the DGSE. The results are shown for four latitude range, 0°−5°, 15°−30°, 30°−45° and 45°−90°, across the north and south Galactic plane. The median values of the C_ℓ for each galactic latitude range are shown by the black vertical lines in each panel. It can be seen that the histogram is mostly peaked around the median values, and we do not find the signature of a 'long-tailed' distribution across any of the latitude values. The distributions of the C_ℓs are similar for all the latitude ranges except at 0°−5° S/N. Here, the distribution is slightly bimodal. This may be an artefact of the complex extended sources present in the Galactic plane, which were not properly removed from the data. The median values are around $\sim 7.5 \times 10^3$ mK^2 in the Galactic plane ($b = 0^{\circ}-5^{\circ}$) and decrease to $\sim 3 \times 10^3$ mK^2 beyond the Galactic plane ($b = 15^{\circ}-30^{\circ}$). For the latitude range $b > 30^{\circ}$, the DGSE becomes much weaker compared with that in the Galactic plane, and the corresponding median C_ℓ values are mostly similar across a wide range of latitudes. As noted earlier, here we are mostly dominated by residual point sources, and measured C_ℓs correspond to an upper limit of DGSE. Subsequently, we investigate how the median C_ℓ changes with ℓ for different Galactic latitude ranges in the Northern and Southern hemispheres.

In order to quantify the possible signature of North and South asymmetry, we considered the measurements of the C_ℓ in the Northern and the Southern hemisphere. We divided the whole latitude range into different parts and compared the median of the C_ℓ values. The left and right panels of Fig. 5 show the variation of the median C_ℓ as a function of ℓ for various latitude ranges. The blue solid line and the red dashed line in the left panel show the median C_ℓ for the galactic latitude range 0°−5° for the Northern and Southern hemisphere, respectively. We found that the median values are almost symmetric for both hemispheres. The results are also very similar for other latitude ranges (30°−45° and 45°−90°). However, there is some asymmetry in the Northern and the Southern hemisphere in the latitude range 15°−30° (right panel of Fig. 5). The overall amplitude is slightly higher for the Northern hemisphere. Moreover, this latitude range (15°−30°) is the transition region from the disc-dominated region to the high-latitude region dominated by the diffuse halo, and our result shows that in the transition region the angular power spectra values are considerably different in the Northern and Southern hemispheres. This may be a result of the complex structure of the disc contributing asymmetrically, or variation of structures resulting from the disc–halo interaction in the two hemispheres, leading to asymmetric structures in the density and magnetic field (Simard-Normandin & Kronberg 1980; Mao et al. 2012). It can also be seen that the median values of C_ℓ are mostly constant beyond $\ell \geq 1500$ in different latitude bins. In the

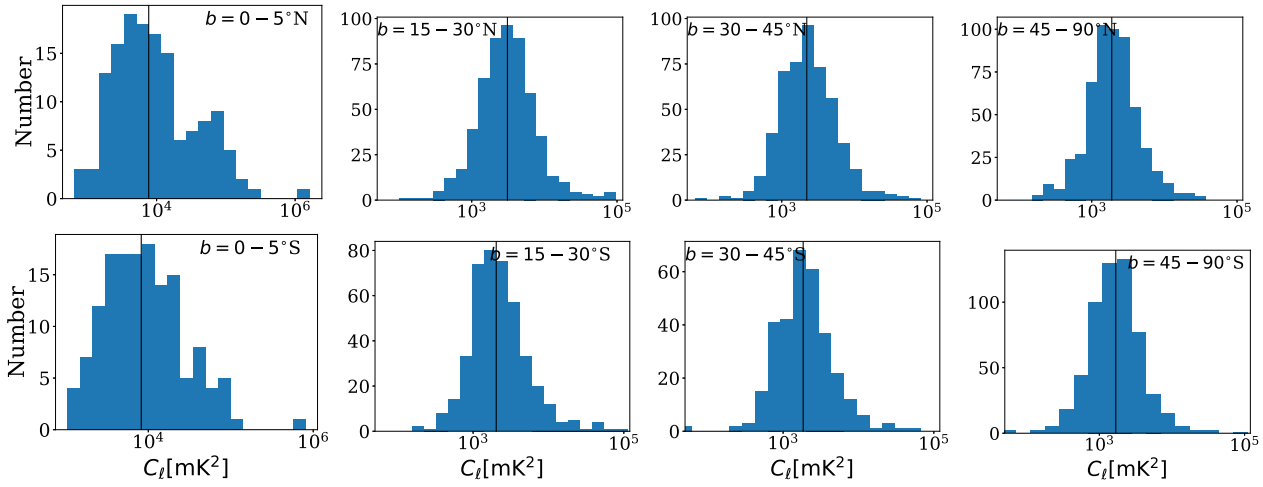

Figure 4. Histograms of the C_ℓ values in various galactic latitude ranges. The upper and lower panels are for the Northern and the Southern hemisphere respectively. The distribution is for a fixed $\ell = 384$. The median value of C_ℓ is shown by the black vertical line in each panel.

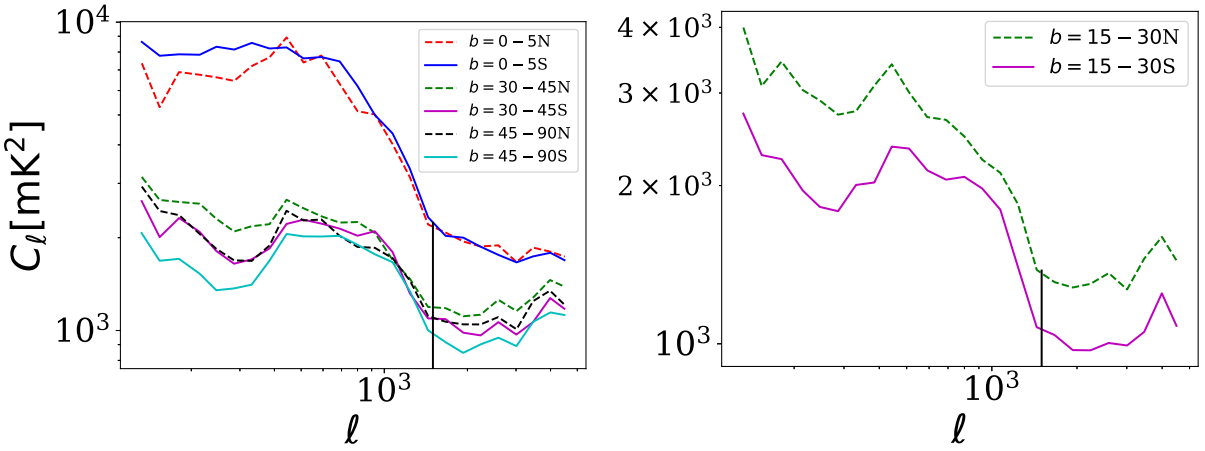

Figure 5. A comparison of the median values of the C_ℓ measurements for the Northern (dashed lines) and Southern (solid lines) hemispheres. The left panel shows the median C_ℓ as a function of ℓ for latitude ranges $b = 0^\circ - 5^\circ$, $30^\circ - 45^\circ$ and $45^\circ - 90^\circ$. The measurements are almost symmetric for the two hemispheres. The right panel shows the comparison in the latitude range $b = 15^\circ - 30^\circ$. In this case, the measured C_ℓ are slightly asymmetric, and the overall amplitude is slightly higher for the Northern hemisphere. This may be due to the complex structure of the disc contributing asymmetrically, or to variation of structures resulting from disc–halo interaction in the two hemispheres, leading to asymmetric structures in the density and magnetic field.

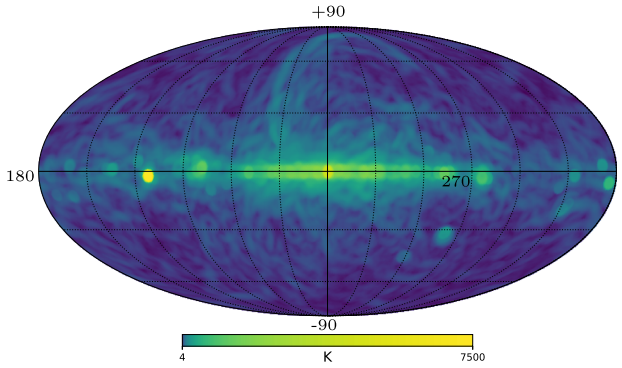

Figure 6. Map of the brightness temperature rms of the DGSE at 150 MHz from an improved all-sky Haslam map. The angular resolution of this map is 13.7 arcmin, which is downgraded from the original 1.7 arcmin in the 408-MHz map (Remazeilles et al. 2015). We used an average spectral index of 2.695 from Platania et al. (2003) to scales at 150 MHz which is relevant for our study. The rms is calculated within a radius of 3° close to the field of view of GMRT at this frequency.

left panel, we detect a higher residual power in the Galactic plane, mostly due to a combination of higher rms noise (fig. 8 in Intema et al. 2017) and residual point sources. The flattening of C_ℓ around the same angular scales ($\sim 0\overset{\circ}{.}12$) for all latitude ranges seems to suggest that the relative contributions of the increase in rms noise and the DGSE are similar as we move away from the Galactic plane.

We also compared the median values of the measured C_ℓ in the North Polar Spur (NPS) ($20 < l < 40$ and $20 < b < 70$) and the Southern hemisphere ($b < -20$). We detected a factor of two increase of the median values for the NPS across all angular scales. In Fig. 6, we see the same feature, where the magnitude of the rms brightness temperature at the NPS is large compared with that in the Southern hemisphere.

4 COMPARISON WITH SINGLE-DISH MEASUREMENTS

In this section, we compare our δT_b maps with single-dish all-sky surveys. The aim is to quantify how much correlation is present between these two types of map; usually, the single-dish maps are more sensitive to large-scale diffuse emission in the sky. Hence, the cross-correlation between the interferometric and signal-dish rms maps will tell us how sensitive the TGSS observations are for detecting the DGSE.

We used the publicly available improved all-sky 408-MHz Haslam map[9] from Remazeilles et al. (2015) with an angular resolution ~7 arcmin, which is relevant for studying the foreground contribution in the 21-cm signal from the EoR. We downgraded the all-sky map to an angular resolution of 13.7 arcmin. This was done solely for ease of computation while minimizing the loss of too much information for our purpose.

We scaled the Haslam map to a lower frequency at 150 MHz from 408 MHz using an average spectral index of 2.695, which is typical for DGSE (Platania et al. 2003). Note that because the single dish measures the brightness temperature (T_b) of the sky, we calculated the rms fluctuations of these maps within a radius of 3°, close to the field of view of the GMRT antenna element at 150 MHz. These rms maps will then give us an equivalent representation of the interferometric observations, which are sensitive to the brightness fluctuations of the temperature maps. The rms map, with an angular resolution of 13.7 arcmin, is shown in Fig. 6. We used this map to cross-correlate with the derived brightness temperature fluctuations from the TGSS measurements.

Next, we investigated the correlation coefficient between the TGSS and the Haslam scaled map at 150 MHz in different longitude and latitude ranges. For the TGSS, we used the map at the multipole $\ell = 246$, or equivalently $\theta \sim 0\overset{\circ}{.}73$. As shown in Fig. 3 (Choudhuri et al. 2017a), the residual map at $\ell = 246$ is free from the convolution of the tapering window and primary beam, and likely to be dominated by the DGSE. Fig. 7 shows the variation of the brightness temperature fluctuations as a function of galactic latitude for various longitude ranges: the longitude range is divided into intervals of 40°, with different ranges shown in different panels. In Fig. 7, the blue dashed lines represent the rms fluctuations from the Haslam map, whereas the red solid lines show δT_b with 1σ error bars from the TGSS survey. Note that we divided the rms of the Haslam

[9] http://www.jb.man.ac.uk/research/cosmos/haslam_map/

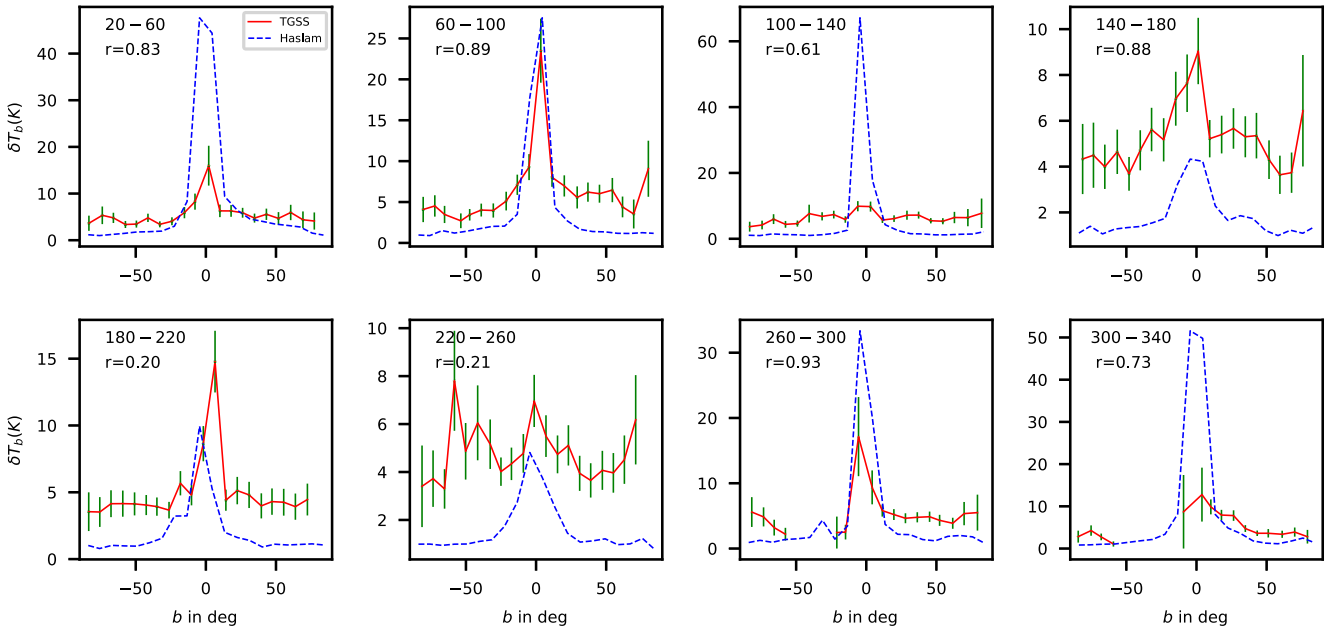

Figure 7. The brightness temperature fluctuations from the Haslam and the TGSS as a function of galactic latitude for various longitude ranges, as indicated in each panel. The value of the angular multipole used for the TGSS is $\ell = 246$, which is free from the convolution of the tapering window and primary beam, and likely to be dominated by the DGSE. Here, the blue dashed lines show the rms of the Haslam map divided by 10, whereas the red solid lines present the $\delta T_{\rm b}$ values with 1σ error bars from the TGSS. The corresponding Pearson product-moment correlation coefficient (r) is also shown in each panel.

map by a factor of 10 in order to obtain a better visualization of the trends of the cross-correlation. For almost all cases, the trend of variation for the TGSS and Haslam map as a function of galactic latitude is quite similar: these curves peak around the Galactic plane and then slowly decrease for higher galactic latitudes. There are also some additional peaks in the TGSS measurements (e.g. at $(l, b) = (220{-}260, -60)$), which we cannot currently explain.

In order to quantify the correlation between the Haslam map and the TGSS, we computed the Pearson product-moment correlation coefficients, defined as $r_{ij} = C_{ij}/(\sqrt{C_{ii} * C_{jj}})$, where C_{ij} is the covariance of x_i and x_j, and the element C_{ii} is the variance of x_i; here, x_i and x_j correspond to the rms of the Haslam map and $\delta T_{\rm b}$ from TGSS. The variation of the correlation coefficient, r, for different galactic longitude ranges is also given in Fig. 7. We find that $r \geq 0.5$ for most of the longitude ranges ($\sim>$ 75 per cent). The relatively higher Pearson product-moment correlation coefficient assures us that at this angular scale ($\theta \sim 0.^{\circ}73$) of the TGSS survey, we are quite sensitive to the large-scale diffuse emission of the Galactic synchrotron emission.

5 SUMMARY AND CONCLUSIONS

In this paper, we have estimated the all-sky angular power spectrum of the temperature fluctuations using the 150-MHz TGSS. The angular resolution for this survey is 25 arcsec × 25 arcsec. The frequency and angular resolution of this survey are relevant for studying the Galactic synchrotron emission, which is one of the main foreground components for detecting the cosmological 21-cm signal from the EoR.

We presented the angular power spectrum C_ℓ measurements of the TGSS, both before and after subtracting the point sources from the data. We found that the measured C_ℓ before point-source subtraction is nearly flat, in the range $10^4{-}10^5$ mK^2, across the measured angular multipoles. This is mainly because of the discrete radio sources, which are distributed isotropically all over the sky. The amplitude of the C_ℓ decreases significantly after subtracting the point sources, and we observed that the amplitude is slightly higher in the Galactic plane in the angular scale range $0.^{\circ}3$ to $0.^{\circ}8$. We expect that the residual C_ℓ is likely to be dominated by the Galactic synchrotron emission at these angular scales. However, in the Galactic plane, there will also be additional contributions from the thermal emission from H II regions, from the non-thermal emission from supernova remnants and from diffuse synchrotron emission. On the other hand, the measured C_ℓ at small angular scales (large ℓ) will be dominated by the unsubtracted point sources in the residual data. We found that the resultant all-sky map around a high angular multipole ($\ell = 3459$ or $\theta \sim 0.^{\circ}052$) is almost isotropic, and the derived brightness temperature varies in the range $50{-}100$ K in different directions.

When investigating the measured $C_{\ell=384}$ across different Galactic latitude ranges, we noticed the C_ℓ is mostly peaked around the median values for all latitude ranges except at lower galactic latitudes. At lower latitudes, the distribution is slightly bimodal, which could be due to the artefacts of the complex extended sources present in the Galactic plane. We found that the DGSE remains significant over a certain range of multipoles in the residual data and that the median values from different latitude ranges decrease beyond the Galactic plane. The median value of C_ℓ due to DGSE saturates beyond $b > 30^{\circ}$, and its amplitude is much lower than on the Galactic plane.

We investigated the north and south asymmetry using the residual data for different latitude ranges. We found that the median C_ℓ as a function of ℓ is almost symmetric for both hemispheres, except in the latitude range $15^{\circ}{-}30^{\circ}$. This latitude range is the transition region from the disc-dominated region to the high-latitude region dominated by the diffuse halo. This may be due to the complex structure of the disc contributing asymmetrically, or to a variation of the structure due to the disc–halo interaction in the two hemispheres, leading to asymmetric structures in the density and magnetic field.

We also found that the C_ℓ measurement in the NPS is almost a factor of two higher than in the southern region of the sky.

When cross-correlating the Haslam and TGSS brightness temperature fluctuations, we detected a correlation coefficient of $r > 0.5$, which suggests that at this angular scale ($0.^\circ3$ to $0.^\circ8$) we are sensitive to large-scale diffuse Galactic synchrotron emission.

Finally, we plan to undertake a detailed all-sky study of the residual C_ℓ as a function of the angular multipole. This will be part of a separate forthcoming paper. We expect the measured C_ℓ to behave as a power law at low angular multipoles ($\ell \leq 550$) and we plan to ascertain the power-law index from the TGSS. This will also enable us to study the variation of the power-law index over different galactic latitude ranges. And this, in turn, can be used to model the DGSE for EoR studies, and to study the magnetic field fluctuations and the ratio of random to ordered magnetic fields in the Galactic plane.

We note that recently Dolfi et al. (2019) and Tiwari, Ghosh & Jain (2019) used TGSS-ADR1 data sets to calculate the clustering properties of radio sources on very large angular scales ($2 < \ell < 30$) and estimated the angular power spectrum from number-count statistics. They found that the amplitude of the TGSS angular power spectrum is significantly higher than that of the NVSS, which cannot be explained by any physically motivated models. The authors indicated that some unknown systematic errors are present in the TGSS-ADR1 data set. Although we are not sensitive to such small angular multipoles using our visibility-based estimators, our results also could be influenced by some systematic flux calibration errors (~ 10 per cent). There may also be various other issues, such as calibration errors, ionospheric distortion, and deconvolution errors during imaging and the point-source subtraction, which are much more significant for low-frequency radio observations. We plan to address these effects with the new release of TGSS-ADR2 data.

ACKNOWLEDGEMENTS

We thank the anonymous referee and the scientific editor for their useful comments and suggestions. SC acknowledge NCRA-TIFR for providing financial support. AG would like to thank the SARAO for support through a SKA postdoctoral fellowship in 2016. Some of the results in this paper were derived using the HEALPY and HEALPIX packages. We would like to acknowledge Mathieu Remazeilles for pointing us to the Haslam map (http://www.jb.man.ac.uk/research/cosmos/haslam_map/). We thank Arianna Dolfi for sharing the TGSS angular two-point correlation function data with us. We thank the staff of the GMRT who made these observations possible. GMRT is run by the National Centre for Radio Astrophysics of the Tata Institute of Fundamental Research.

REFERENCES

Ali S. S., Bharadwaj S., Chengalur J. N., 2008, MNRAS, 385, 2166A
Alvarez H., Aparici J., May J., Olmos F., 1997, A&AS, 124, 205
Baccigalupi C., Burigana C., Perrotta F., De Zotti G., La Porta L., Maino D., Maris M., Paladini R., 2001, A&A, 372, 8
Beardsley A. P. et al., 2016, ApJ, 833, 102
Bennett C. L. et al., 2003, ApJS, 148, 97
Bernardi G. et al., 2009, A&A, 500, 965
Bernardi G. et al., 2010, A&A, 522, A67
Bouchet F. R., Gispert R., 1999, New Astron., 4, 443
Bowman J. D. et al., 2013, PASA, 30, e031
Chakraborty A. et al., 2019, MNRAS, 487, 4102
Cho J., Lazarian A., 2008, preprint (arXiv:0812.2023)
Choudhuri S., Bharadwaj S., Ali S. S., Roy N., Intema H. T., Ghosh A., 2017a, MNRAS, 470, L11
Choudhuri S., Bharadwaj S., Chatterjee S., Ali S. S., Roy N., Ghosh A., 2016b, MNRAS, 463, 4093
Choudhuri S., Bharadwaj S., Roy N., Ghosh A., Ali S. S., 2016a, MNRAS, 459, 151
DeBoer D. R. et al., 2017, PASP, 129, 045001
de Oliveira-Costa A., Tegmark M., Gaensler B. M., Jonas J., Landecker T. L., Reich P., 2008, MNRAS, 388, 247
Di Matteo T., Perna R., Abel T., Rees M. J., 2002, ApJ, 564, 576
Dolfi A., Branchini E., Bilicki M., Balaguera-Antolínez A., Prandoni I., Pandit R., 2019, A&A, 623, A148
Ellingson S. W. et al., 2013, IEEE Trans. Antennas Propagation, 61, 2540
Furlanetto S. R., Oh S. P., Briggs F. H., 2006, Phys. Rep., 433, 181
Gehlot B. K. et al., 2019, MNRAS, 488, 4271
Ghosh A., Bharadwaj S., Ali S. S., Chengalur J. N., 2011, MNRAS, 411, 2426
Ghosh A. et al., 2012, MNRAS, 426, 3295
Giardino G., Banday A. J., Fosalba P., Górski K. M., Jonas J. L., O'Mullane W., Tauber J., 2001, A&A, 371, 708
Giardino G., Banday A. J., Górski K. M., Bennett K., Jonas J. L., Tauber J., 2002, A&A, 387, 82
Ginzburg V. L., Syrovatskii S. I., 1969, ARA&A, 7, 375
Górski K. M., Hivon E., Banday A. J., Wandelt B. D., Hansen F. K., Reinecke M., Bartelmann M., 2005, ApJ, 622, 759
Guzmán A. E., May J., Alvarez H., Maeda K., 2011, A&A, 525, A138
Haslam C. G. T., Klein U., Salter C. J., Stoffel H., Wilson W. E., Cleary M. N., Cooke D. J., Thomasson P., 1981, A&A, 100, 209
Haslam C. G. T., Salter C. J., Stoffel H., Wilson W. E., 1982, A&AS, 47, 1
Iacobelli M. et al., 2013, A&A, 558, A72
Intema H. T., 2014, ASInC, 13, 469
Intema H. T., Jagannathan P., Mooley K. P., Frail D. A., 2017, A&A, 598, A78
Intema H. T., van der Tol S., Cotton W. D., Cohen A. S., van Bemmel I. M., Röttgering H. J. A., 2009, A&A, 501, 1185
Jonas J. L., Baart E. E., Nicolson G. D., 1998, MNRAS, 297, 977
Kerrigan J. R. et al., 2018, ApJ, 864, 131
Koopmans L. et al., 2015, Advancing Astrophysics with the Square Kilometre Array (AASKA14), p. 1
La Porta L., Burigana C., Reich W., Reich P., 2008, A&A, 479, 641
Lazarian A., Pogosyan D., 2012, ApJ, 747, 5
Maeda K., Alvarez H., Aparici J., May J., Reich P., 1999, A&AS, 140, 145
Mao S. A. et al., 2012, ApJ, 755, 21
Mauch T. et al., 2020, ApJ, 888, 61
Mellema G. et al., 2013, Exp. Astron., 36, 235
Morales M. F., Wyithe J. S. B., 2010, ARA&A, 48, 127
Paciga G. et al., 2011, MNRAS, 413, 1174
Paciga G. et al., 2013, MNRAS, 433, 1427
Parsons A. R. et al., 2010, AJ, 139, 1468
Platania P., Burigana C., Maino D., Caserini E., Bersanelli M., Cappellini B., Mennella A., 2003, A&A, 410, 847
Pritchard J. R., Loeb A., 2012, Rep. Prog. Phys., 75, 08690
Regis M., 2011, Astropart. Phys., 35, 170
Reich P., Reich W., 1986, A&AS, 63, 205
Reich P., Reich W., 1988, A&AS, 74, 7
Reich P., Testori J. C., Reich W., 2001, A&A, 376, 861
Reich W., 1982, A&AS, 48, 219
Remazeilles M., Dickinson C., Banday A. J., Bigot-Sazy M.-A., Ghosh T., 2015, MNRAS, 451, 4311
Rybicki G. B., Lightman A. P., 1979, Radiative Processes in Astrophysics. John Wiley & Sons, Hoboken, p. 167
Santos M. G., Cooray A., Knox L., 2005, ApJ, 625, 575
Shaver P. A., Windhorst R. A., Madau P., de Bruyn A. G., 1999, A&A, 345, 380
Simard-Normandin M., Kronberg P. P., 1980, ApJ, 242, 74
Sirothia S. K., Lecavelier des Etangs A., Gopal-Krishna Kantharia N. G., Ishwar-Chandra C. H., 2014, A&A, 562, A108

Swarup G., Ananthakrishnan S., Kapahi V. K., Rao A. P., Subrahmanya C. R., Kulkarni V. K., 1991, Curr. Sci., 60, 95
Tegmark M., Efstathiou G., 1996, MNRAS, 281, 1297
Tegmark M., Eisenstein D. J., Hu W., de Oliveira-Costa A., 2000, ApJ, 530, 133
Tiwari P., Ghosh S., Jain P., 2019, ApJ, 887, 175
van Haarlem M. P. et al., 2013, A&A, 556, A2
Waelkens A. H., Schekochihin A. A., Enßlin T. A., 2009, MNRAS, 398, 1970
Zheng H. et al., 2017, MNRAS, 464, 3486

This paper has been typeset from a TEX/LATEX file prepared by the author.